Faraday Synthesis of Unequally Spaced Data and Complex Deconvolution

W. D. Cotton (NRAO), L. Rudnick (U. Minn) October 21, 2022

***Abstract*—Faraday (AKA "Rotation Measure") synthesis is a technique for extracting information about magnetized plasmas in front of linearly polarized sources. This memo explores this technique using simulated and observed wide-band MeerKAT data. Using a reference wavelength close to zero in calculating the Faraday allows using a narrower restoring beam in Faraday depth than a reference wavelength mid–band for MeerKAT–like data. The limitations of the coverage in λ^2 space, especially the negative portions, limit what can be recovered in the Faraday spectrum. Faraday components closely spaced in Faraday depth can interfere in ways that distort the derived deconvolved Faraday spectrum. Faraday components which are extended in Faraday depth are not well recovered and may appear as a pair of narrow features. Analysis of the MeerKAT L band observations of the galaxy cluster Abell 3395 exhibit large and rapidly variable Faraday components suggesting that the bulk of the Faraday screen is associated with AGN jets.**

***Index Terms*—Faraday Synthesis**

I. Introduction

POLARIZED radio emission may contain information about the magnetic fields in and in front of regions of synchrotron emission which is otherwise difficult to obtain. Faraday rotation in magnetized plasmas in front of polarized sources affects the linear polarization in a very characteristic way. Faraday synthesis is a technique that allows these effects to be studied even in relatively complex cases. This memo evaluates such a technique using the Obit package [1] [1]. Simulated and observed examples using the MeerKAT array are given.

II. Faraday Synthesis

A linearly polarized wave passing through a magnetized plasma will experience a Faraday rotation of the angle of the polarized signal [2]:

$$\Delta\chi \;=\; \lambda^2\; 0.81 \int n_e B_{\|} dr, \tag{1}$$

where λ is the wavelength in m, n_e is the electron density in cm^{-3}, $B_{\|}$is the strength of the component of the magnetic field along the line of sight in μGauss and r is distance in parsec. The concepts of Faraday dispersion and Faraday depth were introduced by [3]. Faraday Synthesis is a technique for examining the Faraday dispersion function (spectrum) along a given sight-line introduced by [3] and further developed by [2]. [4] refines the technique using a complex CLEAN ([5]) to reduce the levels of side-lobes in the Faraday Point Spread Function (FPSF). [6] describe and give a comparison of different variations on Faraday synthesis and related techniques; we adopt their nomenclature in the following.

National Radio Astronomy Observatory, 520 Edgemont Rd., Charlottesville, VA, 22903 USA email: bcotton@nrao.edu

Minnesota Institute for Astrophysics, University of Minnesota, 116 Church St SE, Minneapolis, MN 55455, USA

[1]http://www.cv.nrao.edu/∼bcotton/Obit.html

III. Faraday Synthesis in Obit

The implementation of Faraday Synthesis in Obit allows usage of Q and U images unequally spaced in frequency. The broadband imaging in task MFImage (Sect. III-A) does a joint deconvolution over the entire frequency band while preserving some frequency resolution although unequally spaced in frequency. Such a deconvolution is necessary to maintain high dynamic range in complex fields.

Following the implementation in [4] and unlike [2], the Fourier transform to the Faraday spectrum uses Q+iU rather than (Q+iU)/I. This gives a Faraday spectrum in units of polarized emission rather than fractional polarization and is hence proportional to SNR. However, this does not directly correct for the spectral index of the emission potentially causing effects which are explored further in Section IV-B.

A. Broadband Imaging

Broadband imaging in Obit uses task MFImage which gives a set of frequency bin images approximately of equal fractional bandwidth which are imaged independently but deconvolved jointly. The fractional bandwidth can be adjusted for the needed frequency resolution to cover the width of the Faraday spectrum. Joint deconvolution in Q and U is also allowed [7] which uses the band averaged polarized intensity in each subband to drive the CLEAN. MFImage is described in more detail in [8].

B. Faraday Synthesis

Formally, the Faraday spectrum is the Fourier transform of Q+iU in λ^2 space. In practice, only a portion of λ^2 space can be accessed and, in particular, the negative portion is completely inaccessable. This latter condition represents a fundamental limitation as the Faraday spectrum will, in general, be complex and not necessarily symmetric so the Q+iU function will not be symmetric about λ^2 = 0.

Faraday synthesis is implemented in Obit task RMSyn which is given Q and U spectral cubes and produces a Faraday spectrum cube on a user defined grid of values. Deconvolution is optional as is a correction for a default spectral index.

The Faraday spectrum is approximated using the Fourier series

$$F_k(x,y) \;=\; K \sum_{j=1}^{n} W_j \; e^{-2i\phi_k(\lambda_j^2-\lambda_0^2)} [Q_j(x,y) + iU_j(x,y)] \quad (2)$$

for Faraday depth ϕ_k where W_j is the weight for frequency sub-band j of n, λ_j is the wavelength of frequency sub-band j, λ_0 is the reference wavelength, i is $\sqrt{-1}$ and Q_j and U_j are the Stokes Q and U sub-band images at frequency j. The normalization factor K is $1/\sum_{j=1}^{n} W_j$. W_j may also include a correction for spectral index[2], α:

$$W_j \;=\; w_j e^{-\alpha \log(\nu_j/\nu_0)} \quad (3)$$

where ν_j is the frequency of channel j, ν_0 is the reference frequency and the weight for sub-band j, w_j, is derived from the off–source RMS in the Q_j and U_j images. w_j is zero for frequency bins totally blanked due to RFI filtering, one otherwise.

C. Deconvolution

The Faraday Point Spread Function (FPSF or "Dirty" beam by analogy with interferometric synthesis) depends on the total spanned bandwidth of the data and the location and widths of nonblanked polarization frequency bins as well as the reference wavelength (λ_0) chosen:

$$B_k \;=\; \sum_{j=1}^{n} \; W_j \; e^{-2i\phi_k(\lambda_j^2-\lambda_0^2)}. \quad (4)$$

This function is calculated over twice the extent in ϕ as the Faraday spectrum to allow deconvolution over its full range.

The function drawn for 1% (68 channel) bandwidth polarization resolution with typical flagging for MeerKAT (used in later examples) at L band is given in Figure 1 for two choices of λ_0. Due to the extensive flagging, the side-lobes are relatively high showing the need for deconvolution.

Deconvolution is done on a pixel-by-pixel basis using a complex Högbom [5] CLEAN deconvolution similar in implementation to [4]. The CLEAN proceeds using a user specified loop gain (default 0.1) up to a user specified maximum number of iterations and/or a maximum residual to collect a set of complex delta functions in bins of ϕ_k. The width of the inner real lobe of the FPSF is taken as the true resolution in the data. The residual complex Faraday spectrum is restored with the delta functions convolved with the complex restoring function

$$R_k \;=\; \frac{B_k}{|B_k|} e^{\frac{-(\Delta\phi)^2}{2\sigma^2}} \quad (5)$$

where $\Delta\phi$ is the offset from the ϕ_0 of the peak and σ is the sigma of a Gaussian fitted to the inner, real lobe of B. Examples are given in Figure 1. The modulus of the complex deconvolved/restored spectrum F_k is saved as the output amplitude image and the phase can be optionally saved.

[2]The spectral index is defined as $I_\nu \propto \nu^\alpha$.

D. Reference Wavelength

Equations 2 and 4 contain a reference wavelength, λ_0, which is relatively arbitrary. [2] stated that they found solutions to be more stable when λ_0 was in the bandpass observed, e.g. the weighted average of the data. Their improved stability may be the result of the nature of their frequency coverage. The difficulty is shown in the rapid fringing inside the amplitude envelope in their Figure 3. Subsequent implementations of Faraday synthesis have followed this practice.

A comparison of the complex FPSF functions and the associated restoring beams (see Section III-C) using midband and zero values for λ_0 is given in Figure 1. Using a near zero reference wavelength leads to a higher phase gradient across the FPSF functions and a narrower central real lobe. The MeerKAT L band frequency coverage with zero λ_0 illustrated in Figure 1 left contains only a single real lobe inside the overall envelope so has minimal opportunity for lobe ambiguity while it still has a narrower central real lobe than using a mid–band λ_0. The following development uses a reference wavelength close to zero[3] and the width of the inner real lobe as the width of the restoring function. This represents a form of superresolution.

E. Parallelization

The computation of the various operations are speeded by a combination of SIMD vectorization [9] (AVX and AVX512 implemented via intrinsics) and multi–threading [10]. The synthesis operation is implemented using the ObitCArray (complex array) class which does operations on an image plane basis; the more expensive operations are enhanced using vectorization. The CLEAN operation is implemented using multi–threading.

IV. Simulated Wide Separation Example

A simulated set of Q and U cubes similar to those produced by MFImage for MeerKAT L band data using a 1% fractional bandpass was generated for a pair of components widely separated in Faraday depth. These components are sufficiently separated in ϕ that they are well resolved even in the undeconvolved image. The cubes contain 68 frequency channels and are flagged similarly to typical MeerKAT L band data - roughly half of the channels. The noiseless model consisted of the two components given in Table I. The FPSF is that illustrated in Figure 1 left.

The two orthogonally oriented elliptical Gaussian components produce images which contain regions in which one or the other of the components, or both, have significant contributions. The Q and U cubes were processed using RMSyn producing a cube from -300 to +300 rad m^{-2} with a spacing of 2 rad m^{-2}. Note, neither component peaks at a value of ϕ exactly on a grid value in the output image. A default spectral index of -1.0 was used.

The Faraday spectra, without deconvolution, are shown in Figure 2 for these three cases. While the two components are well resolved and above the sidelobe level, they are not well above the sidelobes.

[3]But not exactly zero to avoid numerical problems.

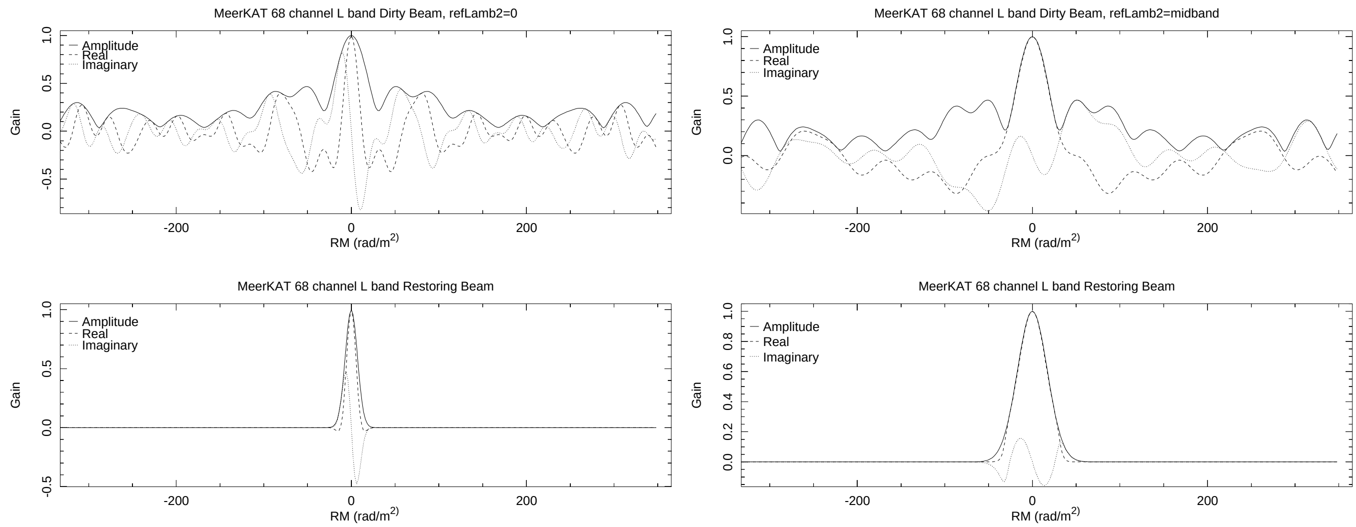

Fig. 1. The MeerKAT 68 channel polarization resolution (1% fractional bandwidth) complex FPSF (upper) and restoring beams (lower). The plots on the left show the results of using a λ_0 near zero and on the right using a λ_0 in the middle of the observed band. The amplitudes are drawn as a solid line, the real part as a dashed line and the imaginary part as a dotted line.

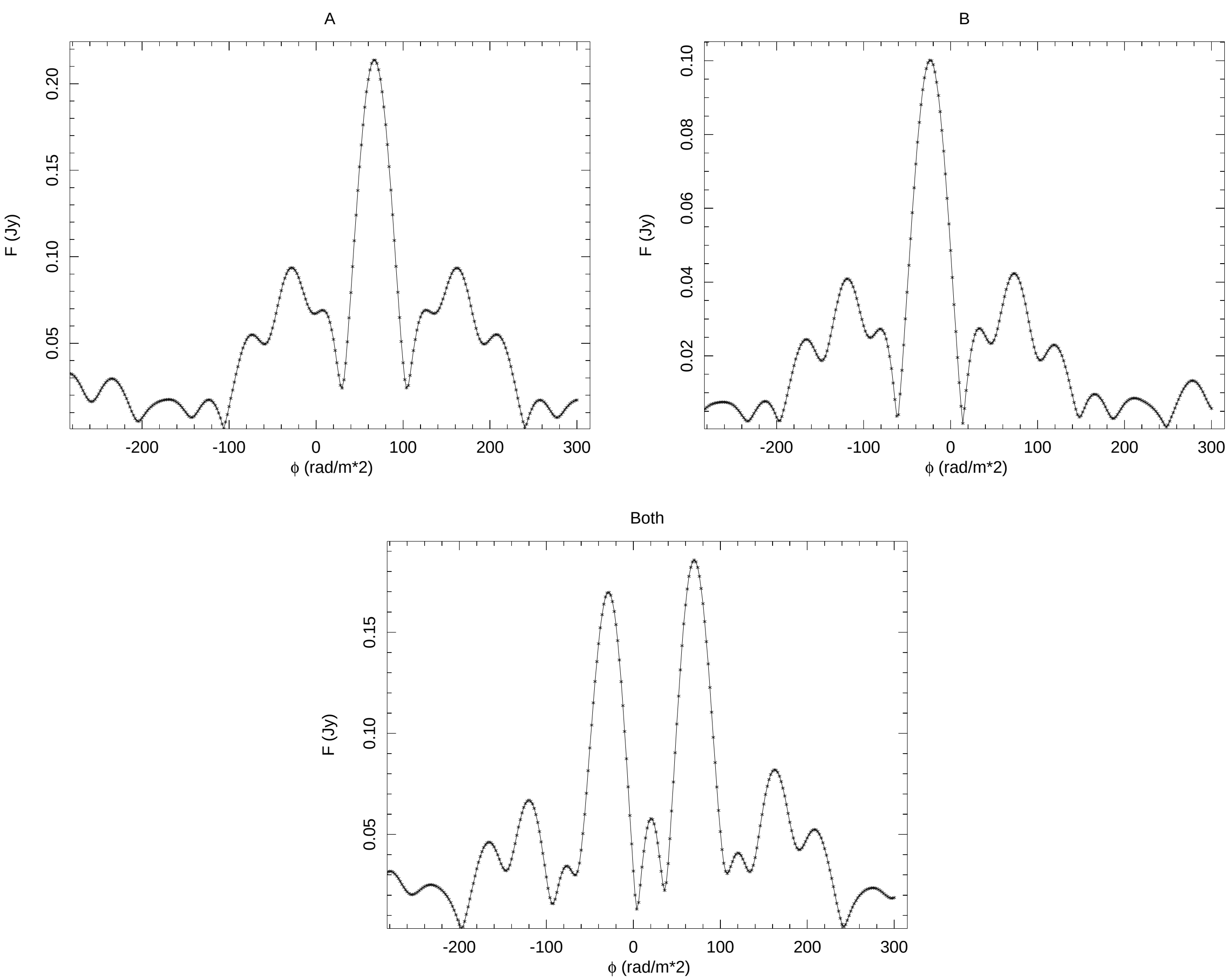

Fig. 2. Simulated MeerKAT data using the model given in Table I without deconvolution. Top left: Position with only component A, Top right: Position with only component B, Bottom: Position with component overlap.

TABLE I
SIMULATED WIDE SEPARATION MODEL

Comp.	I Jy	α	Maj. ”	Min ”	PA °	Q/I ratio	U/I ratio	ϕ rad m^{-2}
A	1.0	-0.4	300	90	-45	+0.15	-0.20	65.
B	0.5	-1.2	200	80	+45	-0.15	+0.20	-25.

TABLE II
MODEL AT SELECTED LOCATIONS

position	pol flux A Jy	pol flux B Jy
A only	0.2073	0.0004
B only	0.0059	0.0897
Both	0.1631	0.1246

A. *Deconvolution*

The test above was repeated but using deconvolution and restoration with a 15.8 rad m^{-2} FWHM Gaussian resulting from a fit to the inner real lobe shown in Figure 1. The results corresponding to Figure 2 are given in Figure 3. A least squares fit to a Gaussian profile was done and the fitted parameters are indicated next to the response in Figure 3. The peak of the response is within a couple rad m^{-2} of the model values for the case where both responses appear and much closer in the cases of only a single response. The fitted Gaussian FWHM is typically comparable to or somewhat larger than the restoring beam size of 15.8 rad m^{-2} The model polarized flux densities are given in Table II which can be compared to the peak values in Figure 3.

It should noted that the default spectral index assumed for this test was α=-1.0 which is different from either component model values given in Table I. The effect of the assumed spectral index is explored further in Section IV-B.

B. *Spectral Index*

Equation 2 for the Faraday spectrum implicitly assumes that the spectral index of the Q and U images is zero. In practice this is seldom the case as polarized emission is most frequently observed in optically thin synchrotron sources which have relatively steep spectra. If uncorrected, a residual spectral index breaks the assumption of a constant intrinsic emitted Q and U and tends to broaden the Faraday spectrum peak. This effect can be compensated by using (Q+iU)/I rather than Q+iU in Equation 2 or by correcting the Q and U spectra for a measured or assumed spectral index. The implementation in RMSyn uses the latter and applies a correction to convert the Q and U pixel values to that at the reference frequency of the image, see Eq. 3. In practice, this will seldom be exactly correct, especially in the case where there are several components with different spectral indices.

The test displayed in Section IV-A was repeated using a range of assumed spectral indices. The results are shown in Figure 4 for the location with both responses and in Table III for the fitted values at each of the 3 locations. For comparison, the “model” values shown in Table III are those expected from the input model.

From Table III the fitted values to the response are not very sensitive to the assumed spectral index at the positions where one component or the other dominates. The same is largely true at the position with both responses for the dominant component (A) but the width of the secondary component (B) is quite sensitive to the assumed spectral index.

V. SIMULATED NARROW SEPARATION EXAMPLE

When components along the same sight-line are sufficiently close in ϕ to be within the main amplitude lobe of the FPSF, their contributions to Q and U will interfere with each other. The phase in Q+iU space of each component is a function of the Polarization Angle (AKA Electric Vector Position Angle = EVPA) at zero wavelength and the phase of the FPSF as a function of ϕ as seen in Figure 1. The effects of the superposition of the signals can be complicated and the result will not be the convolution of the true Faraday spectrum and the FPSF. The details will depend on how nearly aligned (or unaligned) the Q+iU phases are as a function of frequency. Deconvolution in this case will not recover the true Faraday spectrum.

This effect is explored using tests similar to those in Section IV but with components more closely spaced in ϕ, a separation of 20 rad m^{-2}. These tests used two concentric simulated sources with the same shape, the polarized flux density differed by a factor of 2 and a grid of EVPAs was assigned to the weaker component (B?) while the EVPA of the stronger component (A) was held constant. A spectral index, α, of -1.0 was used in all simulations and in calculating the Faraday spectrum. These models are described further in Table IV and the spectra examined are those at the peak position of the sources.

Results for Models A and B08 only are shown in Figure 5. Results of a Gaussian fit to the amplitude spectrum, the EVPA in the closest cell to the amplitude peak and the RMS residual are listed in each plot. The Faraday synthesis of these single component simulations (nearly) recovers the input model. [NB, amplitude a bit high and width a bit low.]

Each combination of component A and one of the component B? from Table IV was simulated and the resulting deconvolved/restored Faraday spectrum at the center of the source was fitted using two Gaussians. The results are shown in Table V and plots at selected values are shown in Figure 6. These results show that the combination of components closely spaced in ϕ depend critically on the difference in intrinsic EVPA. The two Gaussian fits frequently leave large residuals indicating that the results are not well modeled by two delta functions in ϕ.

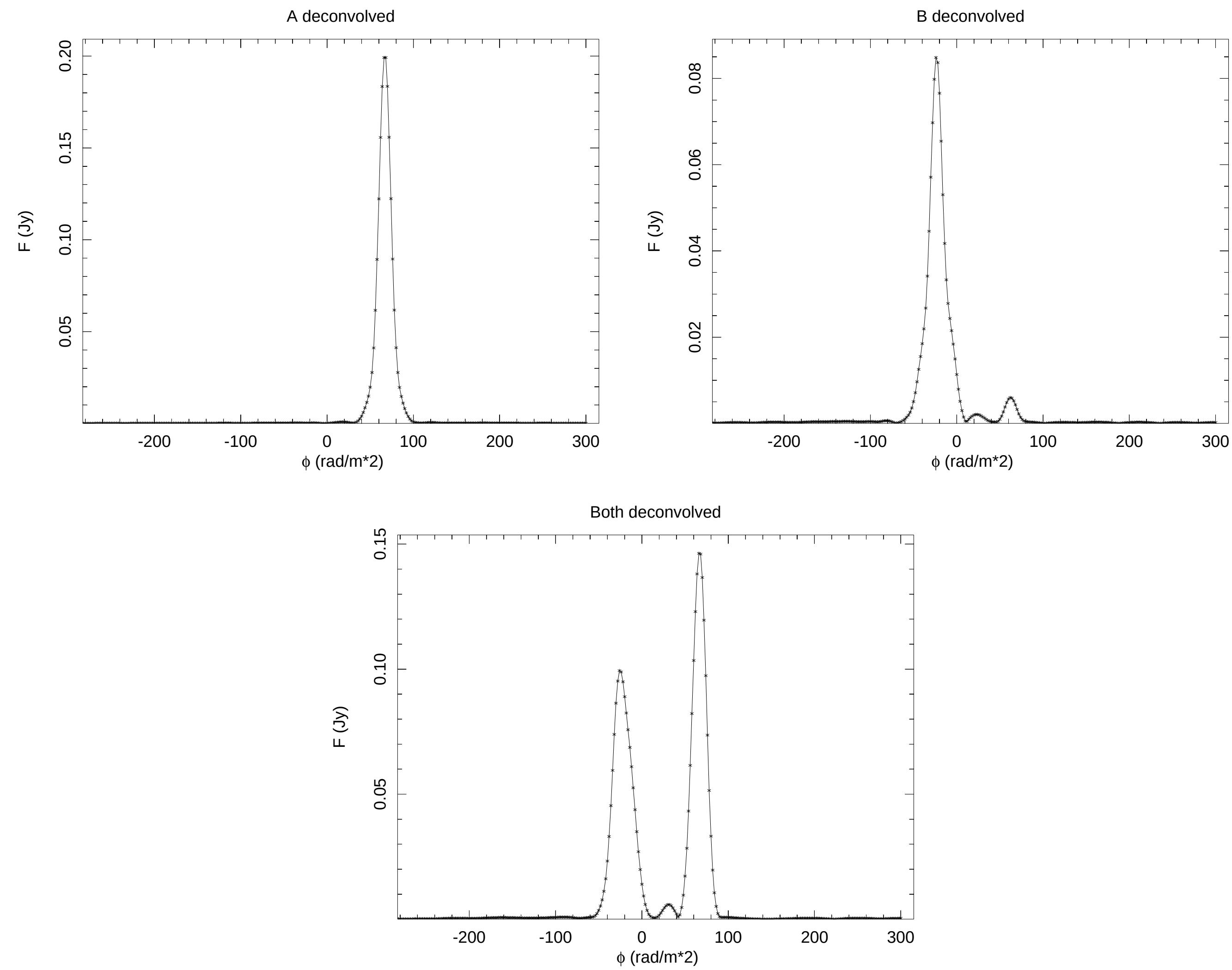

Fig. 3. Simulated MeerKAT data using the model given in Table I with deconvolution. Top left: Position with only component A, Top right: Position with (mostly) only component B, Bottom: Position with component overlap,

TABLE III
MODEL AT VARIOUS SPECTRAL INDICES AND LOCATIONS

α	ϕ A	FWHM A	Peak A	ϕ B	FWHM B	Peak B
	rad m^{-2}	rad m^{-2}	Jy	rad m^{-2}	rad m^{-2}	Jy
0.0	65.3	17.8	0.1969			
-0.5	65.2	17.5	0.1956			
-1.0	65.2	16.7	0.1975			
-1.5	65.2	17.2	0.1990			
model	65.0	15.8	0.2073			
0.0				-30.7	18.4	0.0707
-0.5				-26.4	18.5	0.0702
-1.0				-27.5	17.1	0.0725
-1.5				-27.4	17.1	0.0736
model				-25.0	15.8	0.0897
0.0	64.4	17.8	0.1567	-23.6	20.9	0.1001
-0.5	65.0	17.8	0.1589	-23.0	21.3	0.1022
-1.0	65.0	19.9	0.1579	-23.0	32.6	0.1355
-1.5	65.1	20.5	0.1596	-22.9	36.0	0.1518
model	65.0	15.8	0.1631	-25.0	15.8	0.1246

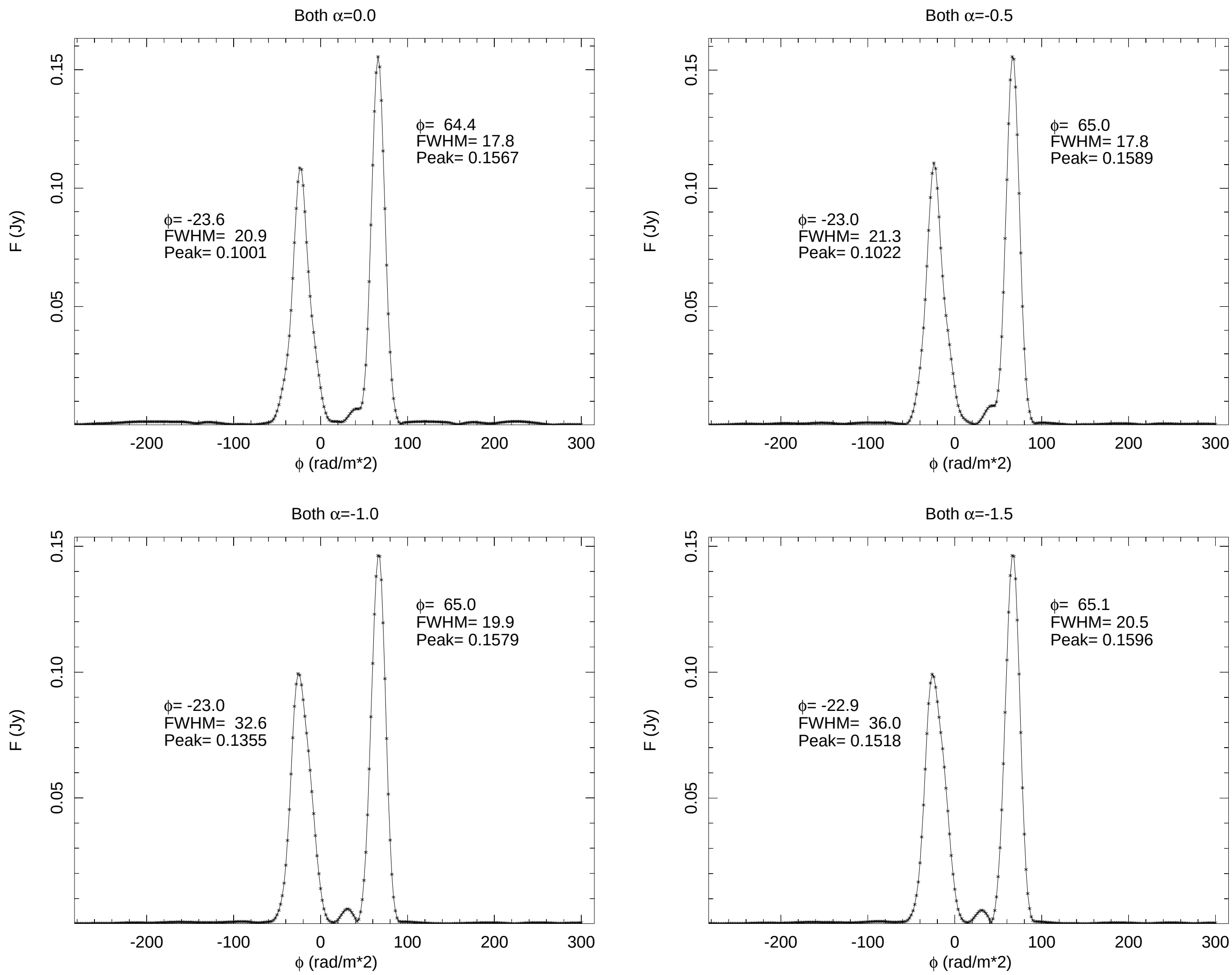

Fig. 4. Simulated MeerKAT data using the model given in Table I with deconvolution and at a position at which both components contribute but with a range of assumed spectral indices. The fitted ϕ of the peak is labeled in rad m^{-2}, the FWHM of the Gaussian and the peak value is labeled beside the response. Top left: α=0, Top right: α=-0.5, Bottom left: α=-1.0, Bottom right: α=-1.5.

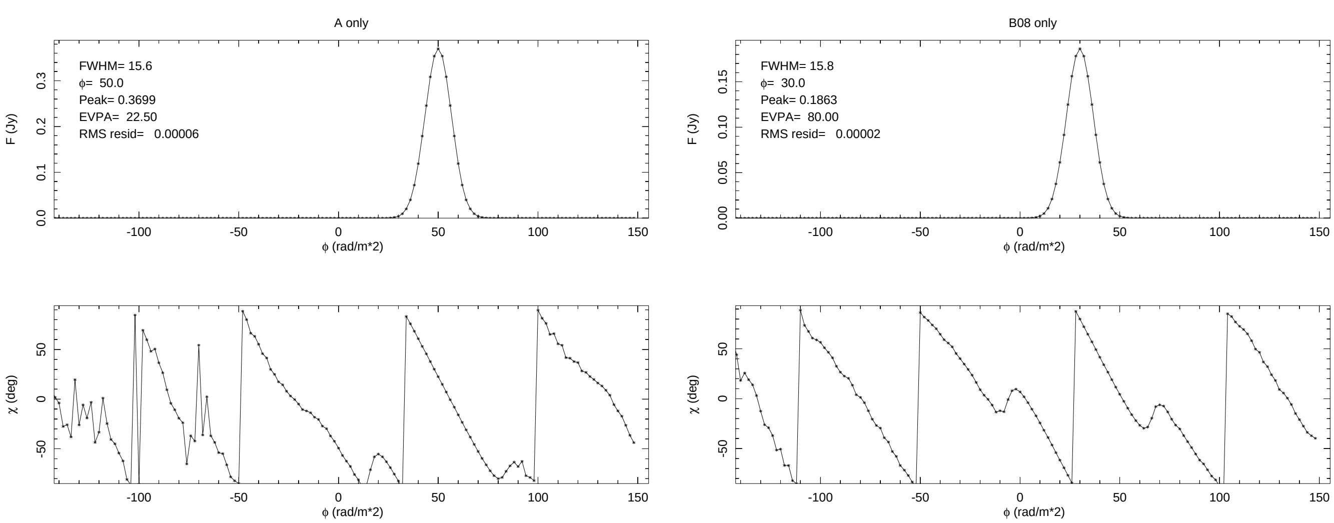

Fig. 5. Simulated MeerKAT data using the models given in Table IV with deconvolution and only a single component. Results of Gaussian fits are shown on the left; upper panel is amplitude and the lower panel the EVPA. Left: Model A, Right Model B08.

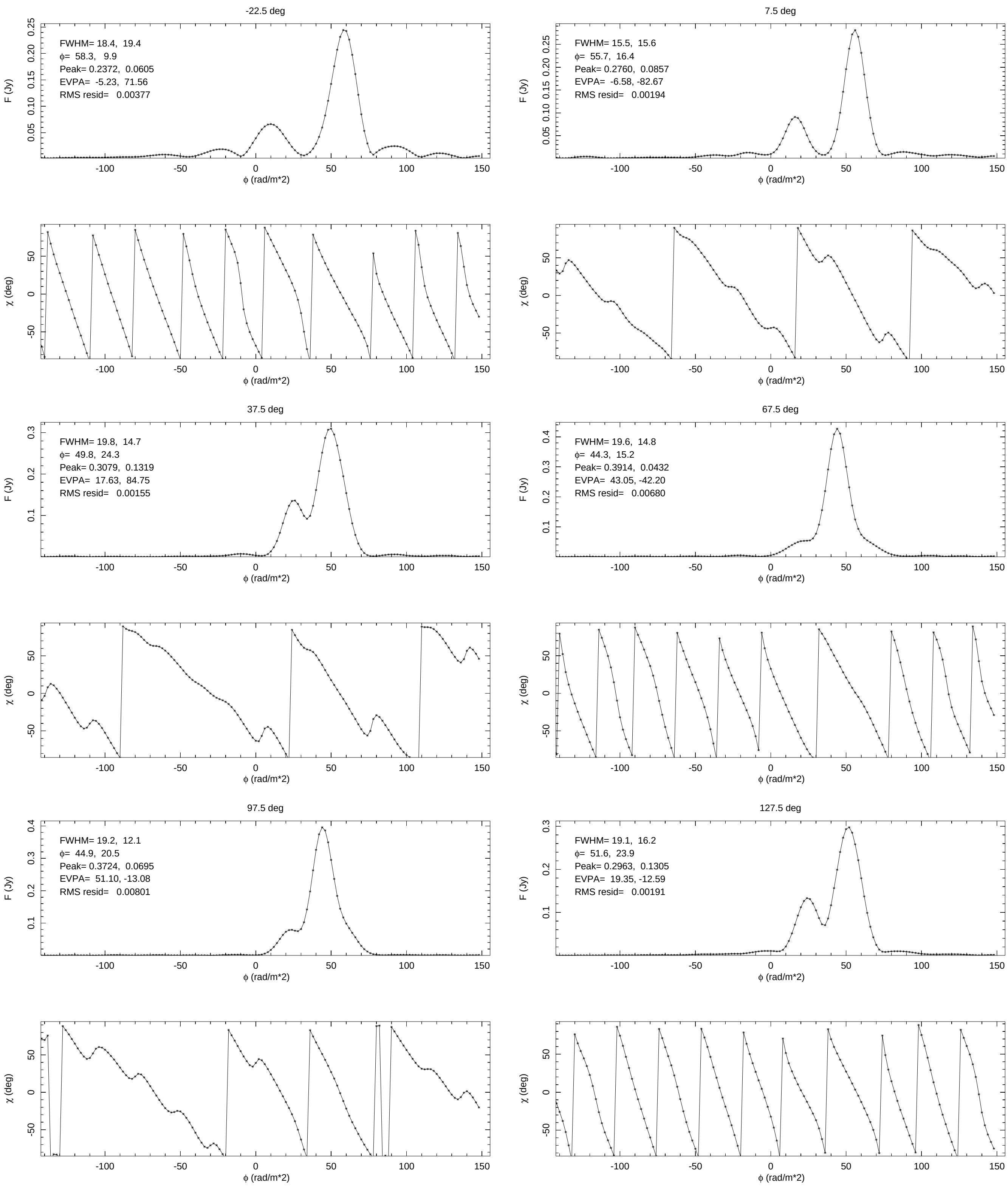

Fig. 6. Simulated MeerKAT data using the models given in Table IV with deconvolution and Component A and one of the Component B?. Results of Gaussian fits are shown on the left for component A, B?; upper panels are amplitude and the lower panels the EVPA. The EVPA offsets are given in the title of each plot. Top left: A-B00, Top right: A-B03, Middle left: A-B06, Middle right: A-B09, Bottom left: A-B12, Bottom right: A-B15.

TABLE V
SIMULATED NARROW SEPARATION FITS

	A				B				
Delta °	FWHM rad m^{-2}	ϕ rad m^{-2}	ppol Jy	EVPA °	FWHM rad m^{-2}	ϕ rad m^{-2}	ppol Jy	EVPA °	RMS Jy
-22.5	18.4	58.3	0.2372	-5.2	29.4	9.9	0.0605	71.6	0.00380
-12.5	16.1	59.2	0.2489	-16.3	16.2	5.5	0.0579	-75.4	0.00310
-2.5	15.9	58.0	0.2493	-12.2	16.2	8.6	0.0631	-66.7	0.00250
7.5	15.5	55.7	0.2760	-6.6	15.6	16.4	0.0857	-82.7	0.00190
17.5	17.1	54.1	0.2860	0.8	25.3	20.9	0.1101	-87.9	0.00370
27.5	23.4	51.9	0.2556	9.4	13.5	22.5	0.1246	89.5	0.00890
37.5	19.8	49.8	0.3079	17.8	14.7	24.3	0.1319	84.8	0.00160
47.5	23.7	47.2	0.3077	25.0	12.8	21.0	0.0912	-74.8	0.00510
57.5	19.9	45.3	0.3603	33.3	13.0	21.2	0.0714	-76.6	0.00530
67.5	19.6	44.3	0.3914	43.0	14.8	15.2	0.0432	-42.2	0.00680
77.5	16.4	43.9	0.4411	45.8	14.8	15.5	0.0385	-26.8	0.00680
87.5	23.0	44.2	0.3660	48.7	19.0	12.3	0.0231	6.1	0.01860
97.5	19.2	44.9	0.3724	51.1	12.1	20.5	0.0695	-13.1	0.00800
107.5	26.8	46.1	0.3042	44.7	15.8	19.6	0.0421	-4.9	0.01190
117.5	30.2	47.9	0.2579	35.8	22.5	19.9	0.0348	-1.7	0.01580
127.5	19.1	51.6	0.2963	19.4	16.2	23.9	0.1305	-12.6	0.00190
137.5	17.6	54.3	0.2884	12.0	19.0	21.8	0.1072	-0.9	0.00310
147.5	19.4	57.9	0.2223	-1.2	18.3	10.3	0.0575	49.6	0.00190

Notes:
Delta is the difference in the model EVPA of components,
FWHM is the Full Width Half Maximum of the fitted Gaussian,
ϕ is the fitted RM of the peak of the Gaussian,
ppol is the fitted peak amplitude of the Gaussian,
EVPA is the EVPA at the nearest cell to the peak of the Gaussian,
RMS is the RMS residual of the two Gaussian fit.

These results are further displayed in Figure 7 which shows the variation of the fitted model Gaussian parameters as a difference in EVPA. The stronger component, A, is less affected by the combination with B but still shows sizable variations in the fitted parameters. The peak ϕ varies smoothly over a range of 15 rad m^{-2} more or less centered on the input model value. Likewise the EVPA smoothly varies over a range of 65° around the model value. The peak amplitude (ppol) varies by a factor of two roughly centered on the model value. The fitted component widths are generally larger than the psf.

The weaker component, B?, is more strongly affected. The peak ϕ values are all at a significantly larger distance from the stronger component than the input model and the peak ppol is systematically lower than the model value. At some differences in intrinsic EVPA, e.g. 67.5 = Figure 6 middle right, the presence of the secondary component is only weakly visible in spite of being half the strength.

The effect of the beating of the two components is illustrated in Figure 8 for a pair of A+B? models which have the maximum difference in the amplitude of component B? in Table V. The top panels, showing the EVPA as a function of λ^2, are very similar as is the fitted single RM with a ϕ nearly half way between that of the two components. The values of EVPA are closely linear with λ^2. However, the runs of fractional polarization with λ^2 are nearly the reverse of each other and quite different from the spectrum of a single component.

VI. TOPHAT SIMULATIONS

Section V has shown that closely spaced but narrow Faraday components with different intrinsic polarization angles present difficulties in reconstruction. In the following, components with finite (tophat) widths in Faraday depths and ranges of ramps in intrinsic polarization angle are examined.

A two dimensional grid of noiseless simulated cases is considered. A tophat distribution in Faraday depth is simulated by using a set of closely spaced (0.25 rad m^{-2}) set of delta functions with the amplitude normalized by the number of these delta functions resulting in a constant total power with tophat width. The tophat widths are 0, 5, 10...50 rad m^{-2} centered on 50 rad m^{-2}; the ramps in EVPA are 0, 10, 20...100° over 50 rad m^{-2}. The spectra for the simulations with an EVPA ramp are shown in Figure 9. The width of the restoring function is 15.8 rad m^{-2}. For tophat widths less than 30 rad m^{-2} the profile is not completely resolved and for widths greater than 35 a double humped profile is seen with the bulk of the emission in the center being resolved out.

An example of the effects of a variable intrinsic EVPA is shown in Figure 10 for the widest (50 rad m^{-2}) tophat function. As the EVPA ramp steepens, the response over the bulk of the center of the tophat function reduces to a near zero level. causing the response to appear as two well resolved component.

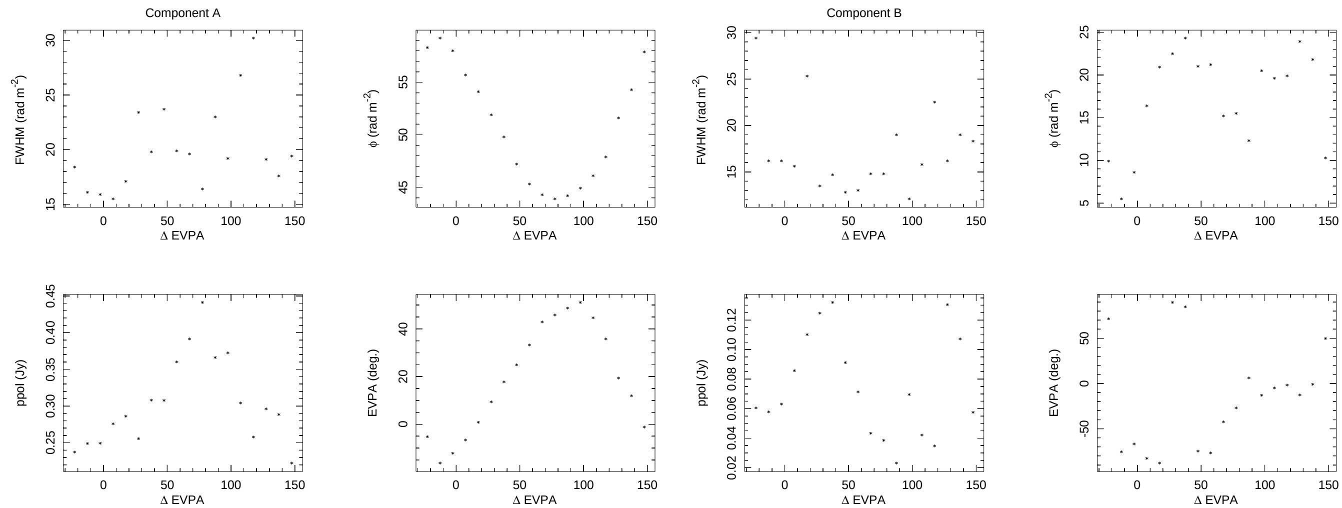

Fig. 7. Fitted Gaussian parameters for the narrow separation tests shown in Table V and Figure 6. Parameters for component A are given in the left set of panels and those for components B? on the right.

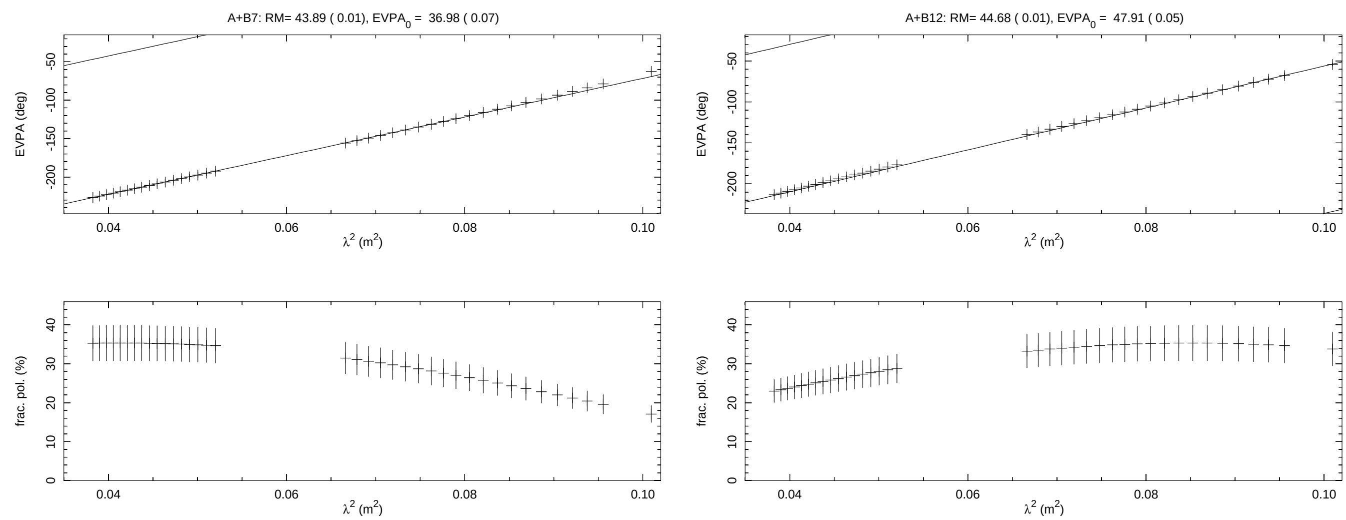

Fig. 8. Q+iU plots in wavelength^2 for two A+B? models. Top panels show the phase expressed as EVPA and the bottom panel the amplitudes as fractional polarization. A single RM is fitted and is drawn in the upper panel as the solid line and the fitted parameters given in the title. Left: Δ EVPA 37.5 which shows the maximum amplitude for Component B07, Right:Δ EVPA 87.5 which shows the minimum amplitude for Component B12 in Table V.

VII. Noise

To facilitate a comparison of the effects of image noise on Faraday synthesis using λ_0 near zero and midband, a sequence of Stokes Q and U images were made with a variable amount of zero mean Gaussian noise added to each voxel in the Q and U image cubes. The source model used was Component B from the test described in Section V. The same image cubes were then subjected to Faraday synthesis using λ_0 near zero and midband. Faraday spectra at the central position of the source for various amounts of noise are shown in Figure 11, and the fitted values are listed in Table VI.

In order to improve the statistics, each test was repeated 100 times and the average RMS recorded in Table VI as <RMS>. The "ratio" column gives the ratio of <RMS> for λ_0 = midband to $\lambda_0 \sim 0$. The noise in the restored spectra for λ_0 = midband is consistently 1.6 times higher than for $\lambda_0 \sim 0$. Fainter components could be detected using λ_0 near zero rather than at midband.

Is this just the difference in restoring beam sizes?

VIII. True Resolution

There is some question about whether the inner, real lobe of the FPSF described in Section III-C or the overall amplitude pattern represents the true resolution. Tests with various levels of added noise to a single component, unresolved in ϕ can help establish the true resolution. The scatter amoung multiple trials of determining the location in ϕ should be a function of the SNR and the true resolution and follow the general scaling

$$\sigma\phi \ = \ FWHM/(2 \times SNR) \qquad (6)$$

where $FWHM$ is the full width at half maximum of the true resolution and SNR the signal to noise ratio. Furthermore, if the resolution resulting from using $\lambda_0 \ \sim 0$ is accurately described by the width of the inner real lobe and the resolution

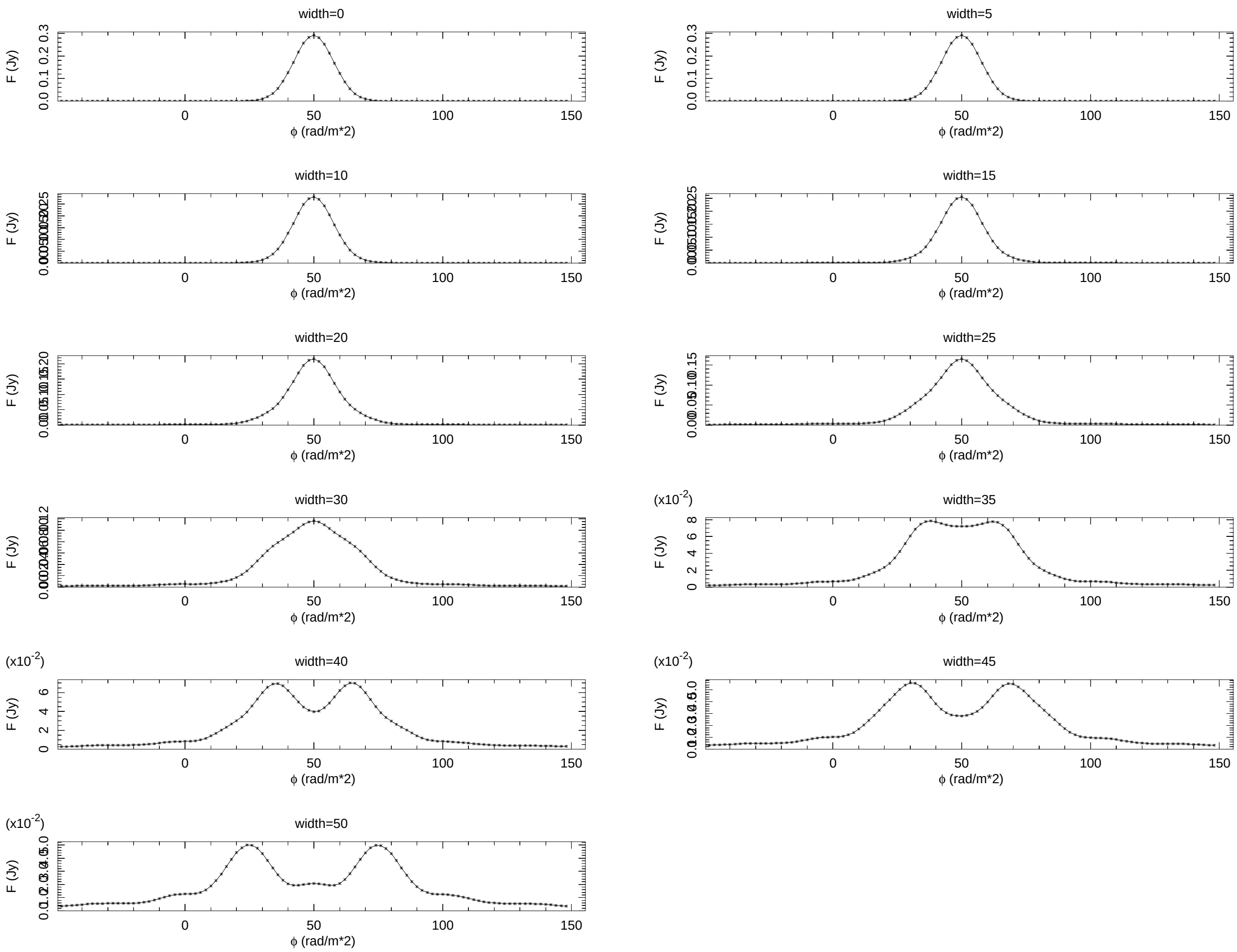

Fig. 9. Faraday spectra of noisless simulations of tophat functions of various widths in Faraday depth. The width is given in the label at the top of each plot. No ramps in EVPA have been added.

TABLE VI
EFFECTS OF ADDED NOISE

	λ_0	~ 0				λ_0	midband				
Noise	FWHM rad m^{-2}	ϕ rad m^{-2}	ppol Jy	RMS Jy	<RMS> Jy	FWHM rad m^{-2}	ϕ rad m^{-2}	ppol Jy	RMS Jy	<RMS> Jy	ratio
0.01	15.8	50.1	0.3692	0.0006	0.00140	47.3	50.1	0.3700	0.0013	0.00226	1.61
0.1	15.6	48.7	0.3588	0.0168	0.01544	39.2	48.4	0.3603	0.0269	0.02556	1.65
0.5	16.9	45.0	0.4106	0.0629	0.07655	37.5	45.8	0.4540	0.1153	0.12318	1.61
0.6	18.4	52.0	0.3247	0.0782	0.08791	39.1	51.0	0.4236	0.1226	0.14068	1.60
0.7	13.2	52.9	0.2781	0.0888	0.09834	49.3	65.5	0.3326	0.1285	0.15973	1.62
0.8	16.9	52.7	0.3969	0.1122	0.12221	37.2	52.8	0.4702	0.1961	0.19722	1.61
0.9	bogus	fit		0.1741	0.12927	bogus	fit		0.2030	0.20973	1.62
1.0	bogus	fit		0.1358	0.14285	bogus	fit		0.2339	0.23096	1.62

Notes:
$\lambda_0 \sim 0$ values are shown on the left, λ_0 = midband on the right.
The "RMS" values were derived from the first half of the spectrum whereas the source response appears in the second.
<RMS> is the average RMS of 100 instances,
ratio is the ratio of <RMS> for λ_0 = midband/$\lambda_0 \sim 0$

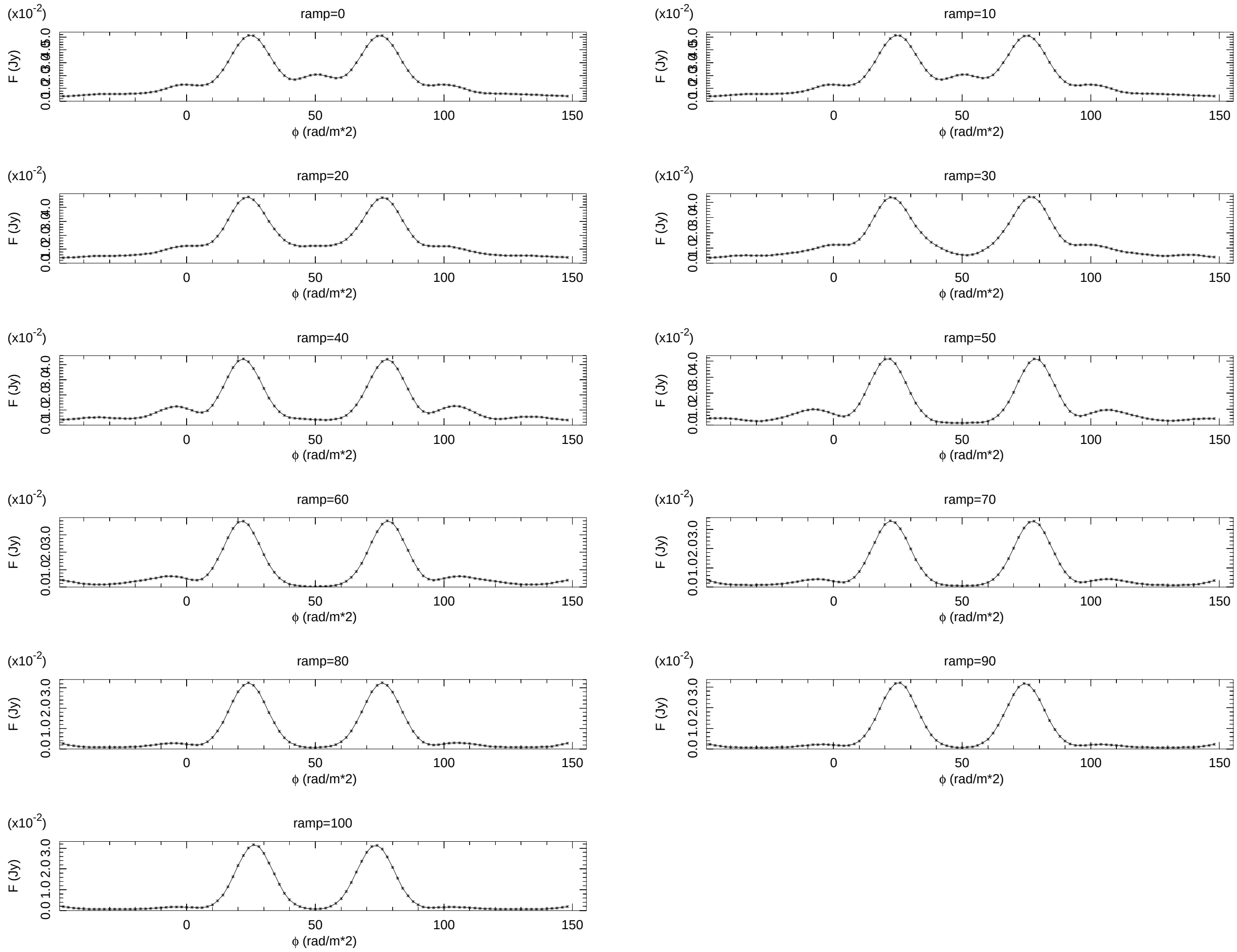

Fig. 10. Faraday spectra of noisless simulations of a 50 rad m^{-2} wide tophat function with various ramps in intrinsic polarization angle (EVPA) across the 50 rad m^{-2}. The EVPAs go from $0°$ to the value given as ramp at the top of each plot in degrees.

using λ_0 at midband is that of the width of the amplitude envelope; this should be reflected in the scatter of the peak ϕ recovered from the two techniques.

A simulation was performed using 400 independent trials of a single component in ϕ with various levels of noise. The simulated Q and U data cubes were then analyzed by RMSyn using both $\lambda_0 \sim 0$ and midband. The test results are shown in Table VII.

According to the position uncertainty scaling law given in Equation 6, the measured uncertainty in Peak ϕ should be proportional to the true resolution. The width of the restoring FPSF function for the λ_0 at midband test is 2.5 times that of the $\lambda_0 \sim 0$ test. Since the same sets of Q and U images are used in both sets of tests, the scatter in the Peak ϕ (9th column) in Table VII for the $\lambda_0 \sim 0$ entries should be less than half that of the λ_0 at midband entries. Instead, they are only marginally smaller.

This small difference could be due largely to the narrower restoring FPSF used in the $\lambda_0 \sim 0$ test. To test this possibility, the $\lambda_0 \sim 0$ test was rerun but using a restoring FPSF the width of the λ_0 at midband test. The results are shown as the last three entries in Table VII. These values for the uncertainty in Peak ϕ are very close to those for the λ_0 at midband test. Usage of $\lambda_0 \sim 0$ and a restoring FPSF the width of the inner real lobe apears not to provide any additional resolution.

IX. Observed Example

MeerKAT observations of the cluster of galaxies J0627.2-5428 (Abell 3395) were reported by [11]; the observations consisted of approximately 9 hours duration, including calibration, at L band (856-1712 MHz). Calibration was described in [11]. The data were imaged in Obit/MFImage with 0.3% fractional bandwidth (123 spectral channels) using joint Q/U deconvolution. A Faraday spectrum cube was generated using RMSyn with 2 rad m^{-2} sampling between -800 and +600 rad m^{-2} and deconvolved/restored as described above. A Stokes I contour plot of a portion of the cluster is given in Figure 12 which indicates the locations given in Faraday spectrum plots in Figures 13 and 14. These plots show a single, unresolved component in several background AGNs and the halo(?) in the cluster but mostly very complex structure for the locations in prominent cluster AGNs, LEDA 19057 and LEDA 19029. The southernmost sample in LEDA 19057 has primarily only

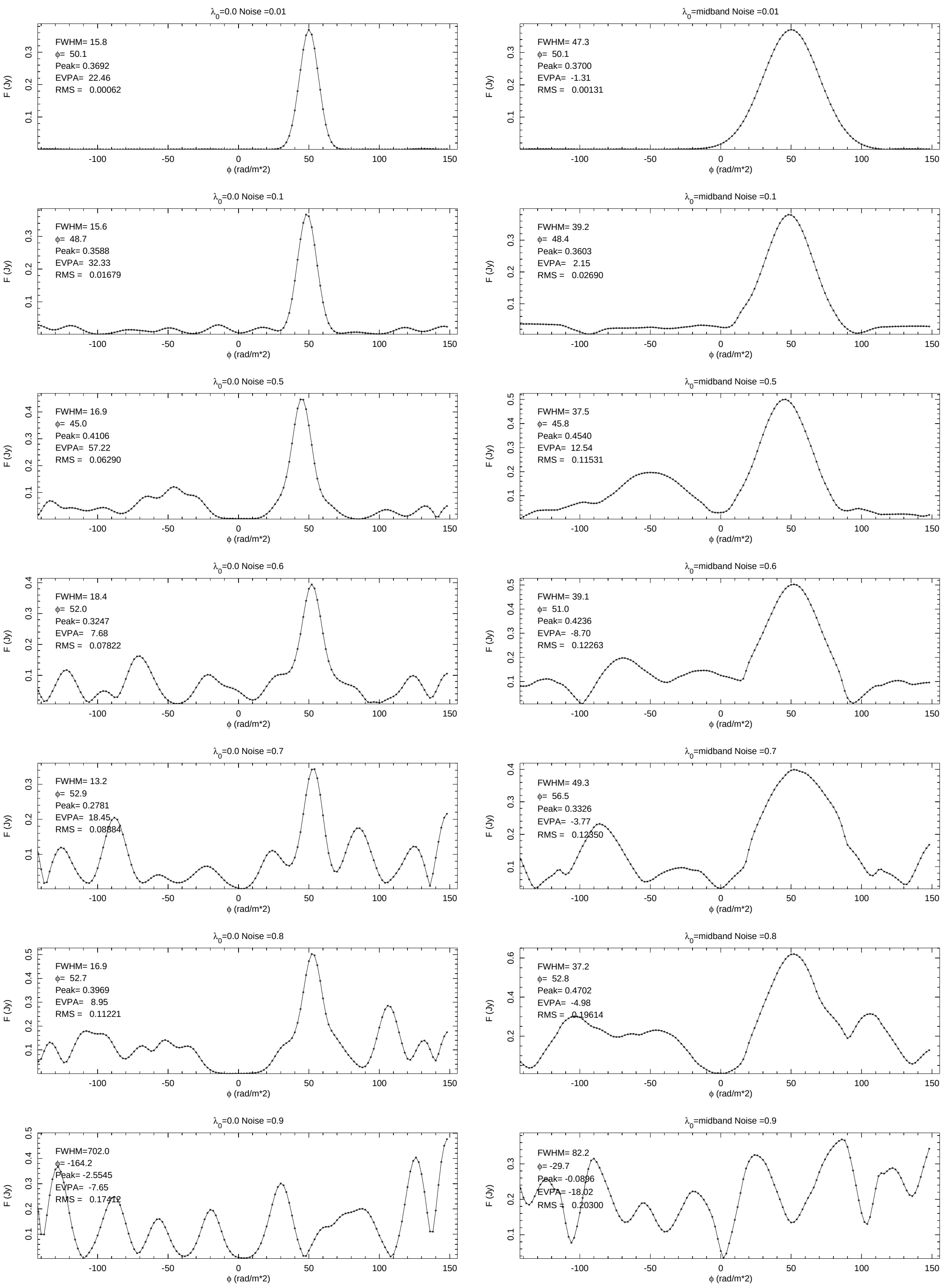

Fig. 11. Comparison of the effect of increased noise on using λ_0 near zero left panels or midband (right panels). From the top, the added noise values are 0.01, 0.1, 0.5, 0.6, 0.7, 0.8, 0.9. The same noise was used for λ_0 near zero and midband.

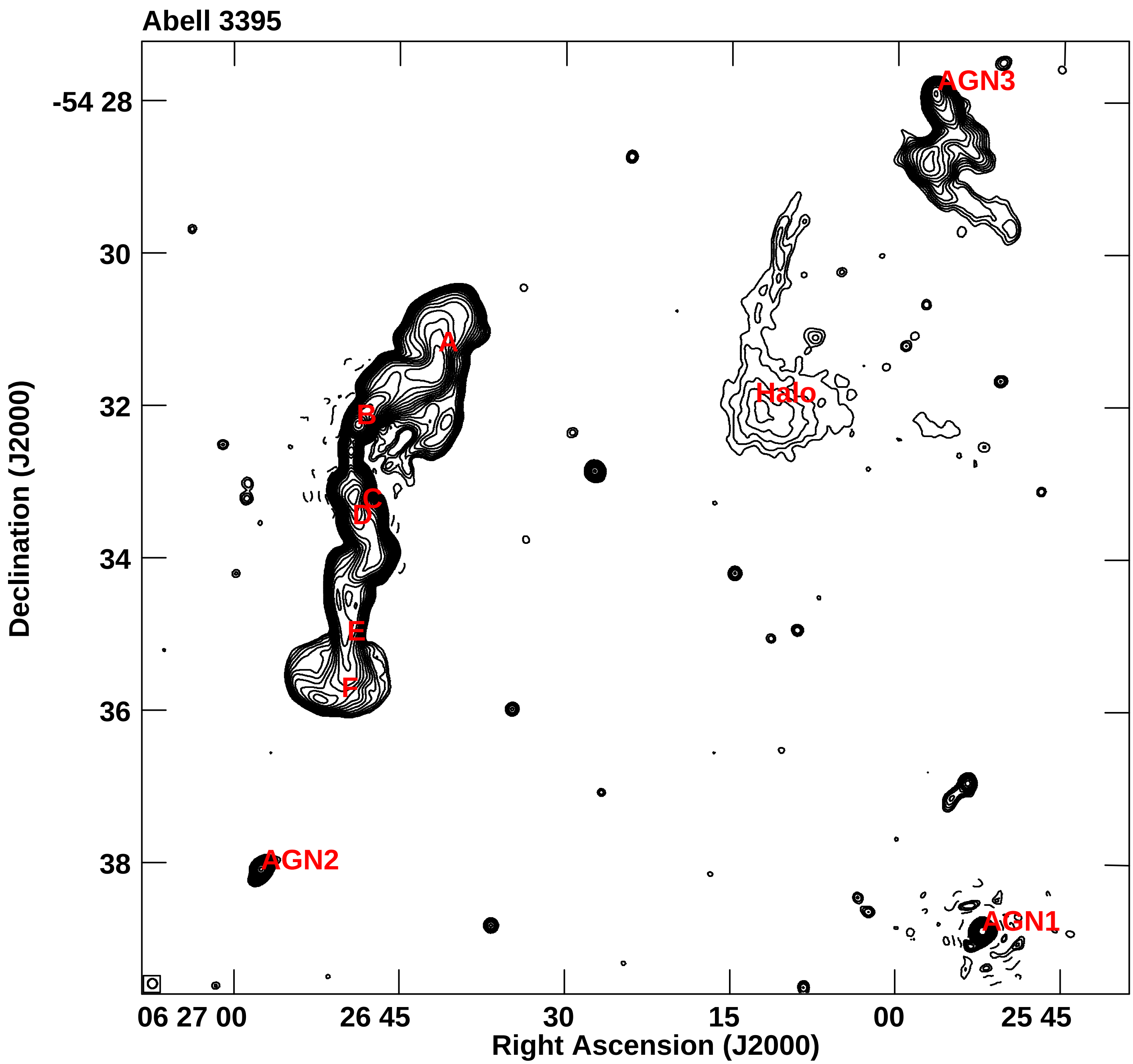

Fig. 12. Stokes I contours of a region of the cluster Abell 3395 with red labels showing the approximate location of RM plots.

TABLE VII
TEST OF TRUE RESOLUTION

λ_0	Noise Jy	Restore σ rad m^{-2}	Peak σ rad m^{-2}	$\pm$	Peak Flux Jy	$\pm$	Peak ϕ rad m^{-2}	$\pm$	RMS Jy
0	0.05	6.71	7.93	0.05	0.360	0.008	49.99	0.19	0.006
0	0.5	6.71	8.16	0.46	0.290	0.070	49.82	1.96	0.057
0	0.7	6.71	8.84	0.62	0.293	0.010	50.17	2.48	0.081
midband	0.05	17.3	20.05	0.17	0.363	0.006	49.99	0.21	0.008
midband	0.5	17.3	17.72	1.75	0.294	0.073	49.87	1.80	0.084
midband	0.7	17.3	18.49	2.31	0.264	0.102	49.88	3.33	0.116
0	0.05	17.3	20.05	0.17	0.363	0.006	49.99	0.21	0.008
0	0.5	17.3	17.72	1.75	0.294	0.073	49.87	1.80	0.084
0	0.7	17.3	18.49	1.88	0.264	0.102	49.88	3.15	0.116

Notes:
Noise is the sigma of the zero mean Gaussian noise added to each cell in the Q and U cubes,
Restore σ is the sigma of the envelope of the restoring beam,
Peak σ is the fitted Gaussian sigma of the width of the component,
Peak Flux is the fitted maximum of the component,
Peak ϕ is the fitted peak ϕ of the component,
RMS is the RMS amplitude noise in the Faraday spectrum away from the added component.
Uncertainties ($\pm$) are the RMS of the population.

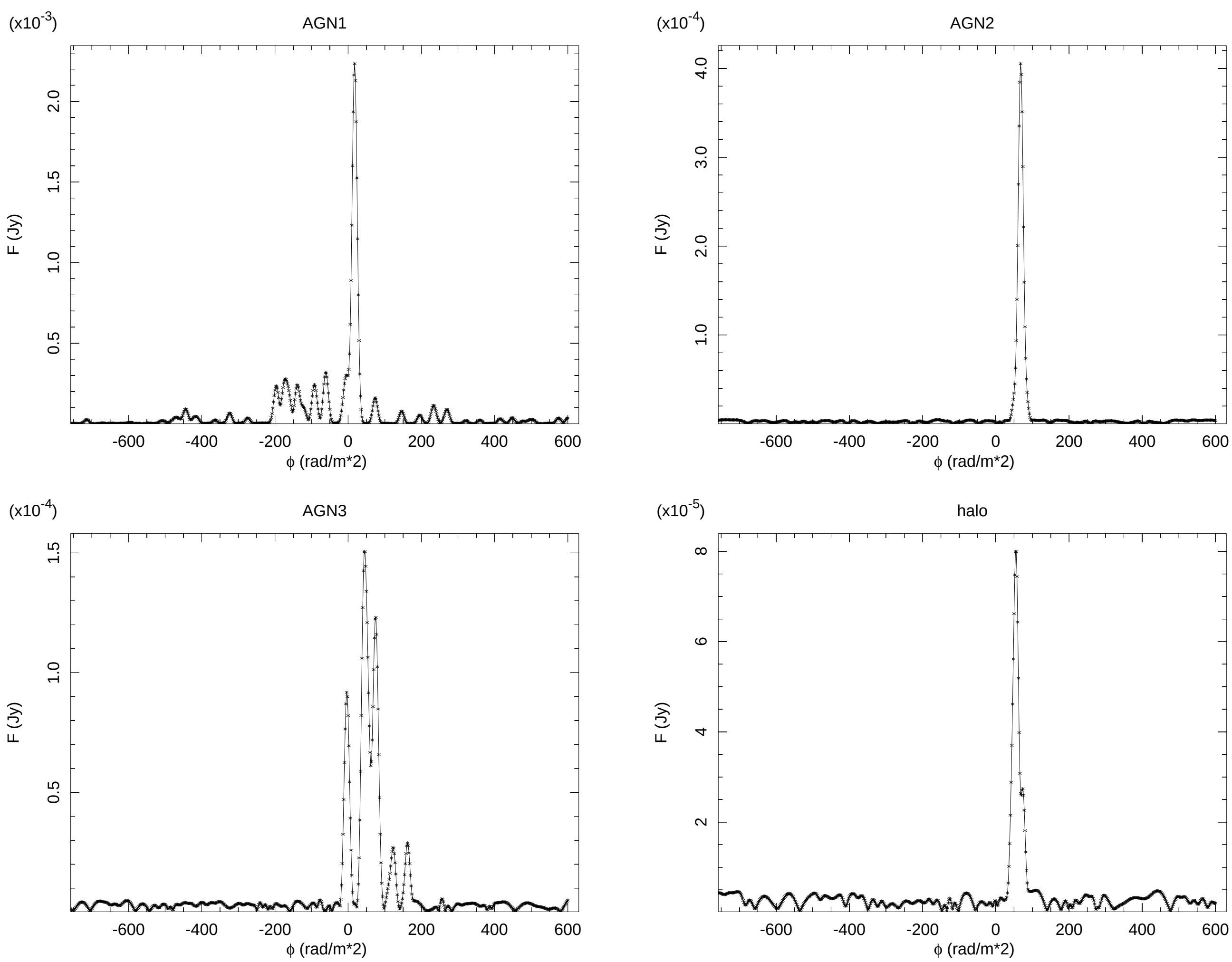

Fig. 13. Faraday depth plots of several sources in the field of Abell 3395 as shown in Figure 12. Top left: AGN1, top right: AGN2, bottom left: AGN3 (LEDA 19029), bottom right: Halo.

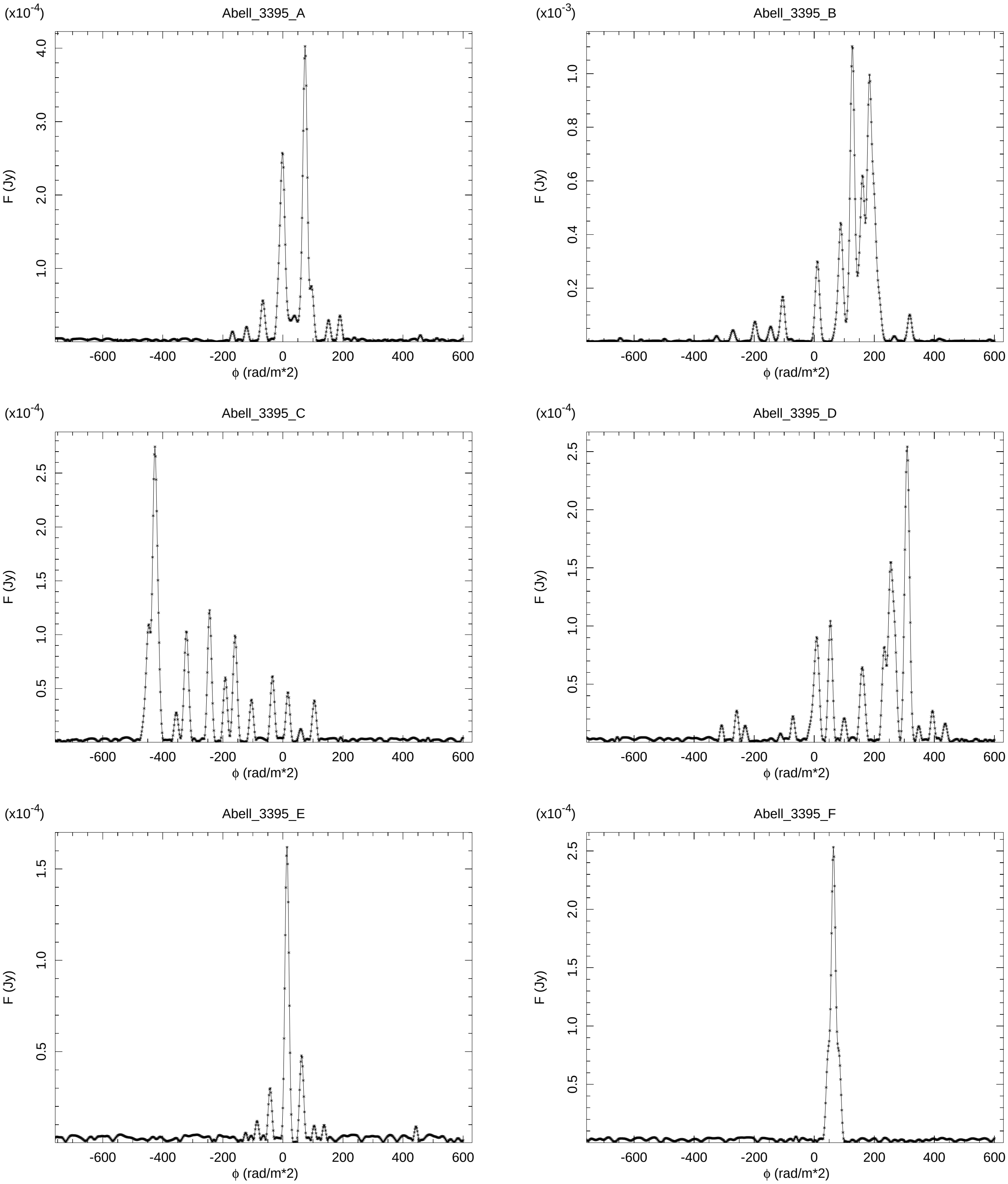

Fig. 14. Faraday spectrum plots of locations in the prominent FRI galaxy (LEDA 19057) in Abell 3395 as shown in Figure 12. Top left: A, top right: B, middle left: C, middle right: D, bottom left: E, bottom right: F.

TABLE IV
SIMULATED NARROW SEPARATION MODEL

Comp.	ϕ rad m^{-2}	I Jy	ppol/I ratio	EVPA °
A	50	1.0	0.353	22.5
B00	30	0.5	0.177	0
B01	30	0.5	0.177	10
B02	30	0.5	0.177	20
B03	30	0.5	0.177	30
B04	30	0.5	0.177	40
B05	30	0.5	0.177	50
B06	30	0.5	0.177	60
B07	30	0.5	0.177	70
B08	30	0.5	0.177	80
B09	30	0.5	0.177	90
B10	30	0.5	0.177	100
B11	30	0.5	0.177	110
B12	30	0.5	0.177	120
B13	30	0.5	0.177	130
B14	30	0.5	0.177	140
B15	30	0.5	0.177	150
B16	30	0.5	0.177	160
B07	30	0.5	0.177	170

a single component. Note: the results of residual instrumental polarization tends to appear around ϕ=0.

Polarized flux density weighted color coded RM images of several cluster features are shown in Figures 15 and 16. Figure 15 shows a wide range, $\pm$ 400 rad m^{-2}, of Faraday depths especially in the southern part of the jet in LEDA 19057. The mixture of positive and negative Faraday depths indicate multiple magnetic field reversals.

Figure 16 shows a relatively simple Faraday depth structure covering the halo in the south with a more complex structure over the AGN to the north. Note: the range of Faraday depth in this images is much less than in Figure 15. The rapid variations of Faraday depth with multiple features along the same sight-line in the cluster AGNs shown in Figures 13 - 16 contrast sharply with the essentially constant Faraday depth to the halo show that much of the Faraday screen is associated with the AGN jets.

X. DISCUSSION

We have presented a technique for determining the Faraday spectrum in radio images and have provided examples of its application to simulations and MeerKAT observations.

The effective resolution of the FPSF in Faraday depth appears not to depend on the reference wavelength, λ_0, used in calculating the spectrum. However, in a form of superresolution, using a λ_0 near zero and a restoring beam the width of the inner real lobe of the FPSF results in a narrower restoring function than using a λ_0 near the middle of the observed frequency spectrum.

The limited range of observations in λ^2 space limits the ability of Faraday synthesis to recover the true distributions in Faraday depth. In particular, the inaccessability of negative λ^2 space can be a serious problem. Since the Faraday spectrum will in general be complex and not necessarily symmetric about ϕ = 0, the Q+iU function will not generally be symmetric in λ^2 space.

The results on the simulated data for widely separated components recovered parameters close to the input model, especially in pixels with only a single component. The polarized flux densities appear to be under estimated and the width of the response in Faraday depth over estimated. An incorrect assumed spectral index of the emission will broaden the response in Faraday depth.

When there are several Faraday components within the central lobe of the FPSF, the results are more complicated. The components interfere with each other and produce a spectrum that depends on the relative polarization angle (EVPA) of the components. The strongest component will be less affected than weaker components. The Faraday spectrum can show the presence of multiple components in a given narrow range of Faraday depth, ϕ, but tends to obscure the details.

Tests using an extended, tophat, distribution in ϕ reveal additional difficulty in recovering the true distribution. When the width is less that the width of the FPSF, the resultant function is a single, peaked response. As the width increases, the response breaks up into a double peaked function. This response is further complicated if there is a substantial variation in EVPA across the tophat.

The MeerKAT observations of galaxy cluster Abell 3395 show a rich variety of features in the Faraday spectrum in the two cluster AGN but only a single, unresolved component in background AGNs and essentially no variation over the cluster halo. The apparent inability to recover extended emission features may be limiting the results in this galaxy to appear as multiple, relatively compact features.

ACKNOWLEDGMENT

We would like to thank Sasha Plavin and George Heald for enlightening discussions.

REFERENCES

[1] W. D. Cotton, “Obit: A Development Environment for Astronomical Algorithms,” *PASP*, vol. 120, pp. 439–448, 2008.

[2] M. A. Brentjens and A. de Bruyn, “Faraday rotation measure synthesis,” *A&A*, vol. 441, pp. 1217–+, Sep. 2005.

[3] B. J. Burn, “On the depolarization of discrete radio sources by Faraday dispersion,” *MNRAS*, vol. 133, p. 67, Jan. 1966.

[4] G. Heald, R. Braun, and R. Edmonds, “The Westerbork SINGS survey. II Polarization, Faraday rotation, and magnetic fields,” *A&A*, vol. 503, no. 2, pp. 409–435, Aug. 2009.

[5] J. A. Högbom, “Aperture Synthesis with a Non-Regular Distribution of Interferometer Baselines,” *A&A Suppl.*, vol. 15, p. 417, Jun. 1974.

[6] X. H. Sun, L. Rudnick, T. Akahori, C. S. Anderson, M. R. Bell, J. D. Bray, J. S. Farnes, S. Ideguchi, K. Kumazaki, T. O’Brien, S. P. O’Sullivan, A. M. M. Scaife, R. Stepanov, J. Stil, K. Takahashi, R. J. van Weeren, and M. Wolleben, “Comparison of Algorithms for Determination of Rotation Measure and Faraday Structure. I. 1100-1400 MHz,” *AJ*, vol. 149, no. 2, p. 60, Feb. 2015.

[7] J. J. Condon, W. D. Cotton, S. V. White, S. Legodi, S. Goedhart, K. McAlpine, S. M. Ratcliffe, and F. Camilo, “Threads, Ribbons, and Rings in the Radio Galaxy IC 4296,” *ApJ*, vol. 917, no. 1, p. 18, Aug. 2021.

[8] W. D. Cotton, J. J. Condon, K. I. Kellermann, M. Lacy, R. A. Perley, A. M. Matthews, T. Vernstrom, D. Scott, and J. V. Wall, “The Angular Size Distribution of μJy Radio Sources,” *ApJ*, vol. 856, no. 1, p. 67, Mar. 2018.

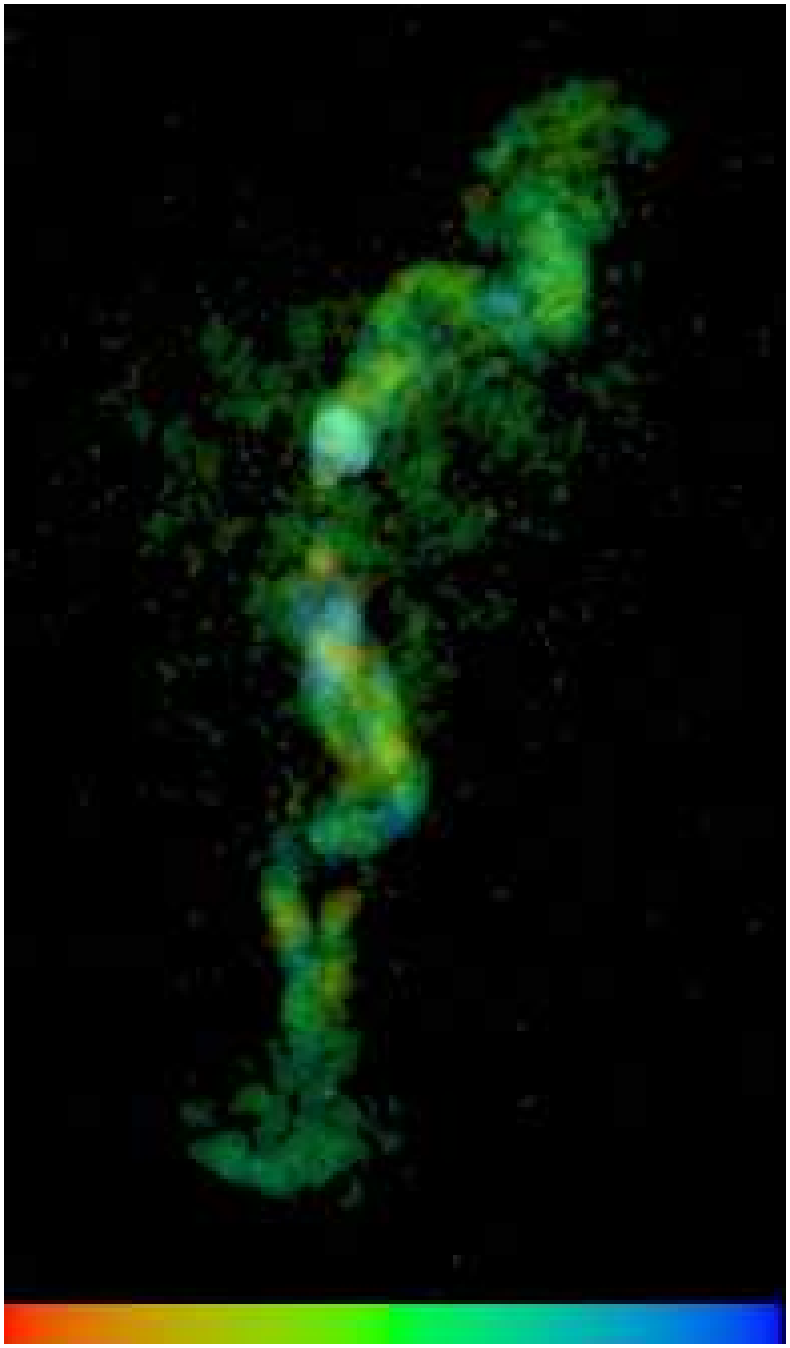

Fig. 15. Polarized intensity weighted color-coded RM image of the prominent FRI galaxy in Abell 3395 (on the left of Figure 12) with color bar at bottom. Stretch is $\sqrt{}$, red is -400 rad m^{-2} and blue is +400 rad m^{-2}. Colors not shown on the bar indicate emission at a range of Faraday depths.

[9] W. D. Cotton, “Notes on icc and AVX,” *Obit Development Memo Series*, vol. 61, pp. 1–2, 2019. [Online]. Available: ftp://ftp.cv.nrao.edu/NRAO-staff/bcotton/Obit/ICCAVX.pdf

[10] ——, “Note on the Efficacy of Multi-threading in Obit,” *Obit Development Memo Series*, vol. 1, pp. 1–8, 2008. [Online]. Available: ftp://ftp.cv.nrao.edu/NRAO-staff/bcotton/Obit/Thread.pdf

[11] K. Knowles, W. D. Cotton, L. Rudnick, F. Camilo, S. Goedhart, R. Deane, M. Ramatsoku, M. F. Bietenholz, M. Brüggen, C. Button, H. Chen, J. O. Chibueze, T. E. Clarke, F. de Gasperin, R. Ianjamasimanana, G. I. G. Józsa, M. Hilton, K. C. Kesebonye, K. Kolokythas, R. C. Kraan-Korteweg, G. Lawrie, M. Lochner, S. I. Loubser, P. Marchegiani, N. Mhlahlo, K. Moodley, E. Murphy, B. Namumba, N. Oozeer, V. Parekh, D. S. Pillay, S. S. Passmoor, A. J. T. Ramaila, S. Ranchod, E. Retana-Montenegro, L. Sebokolodi, S. P. Sikhosana, O. Smirnov, K. Thorat, T. Venturi, T. D. Abbott, R. M. Adam, G. Adams, M. A. Aldera, E. F. Bauermeister, T. G. H. Bennett, W. A. Bode, D. H. Botha, A. G. Botha, L. R. S. Brederode, S. Buchner, J. P. Burger, T. Cheetham, D. I. L. de Villiers, M. A. Dikgale-Mahlakoana, L. J. du Toit, S. W. P. Esterhuyse, G. Fadana, B. L. Fanaroff, S. Fataar, A. R. Foley, D. J. Fourie, B. S. Frank, R. R. G. Gamatham, T. G. Gatsi, M. Geyer, M. Gouws, S. C. Gumede, I. Heywood, M. J. Hlakola, A. Hokwana, S. W. Hoosen, D. M. Horn, J. M. G. Horrell, B. V. Hugo, A. R. Isaacson, J. L. Jonas, J. D. B. Jordaan, A. F. Joubert, R. P. M. Julie, F. B. Kapp, V. A. Kasper, J. S. Kenyon, P. P. A. Kotzé, A. G. Kotze, N. Kriek, H. Kriel, V. K. Krishnan, T. W. Kusel, L. S. Legodi, R. Lehmensiek, D. Liebenberg, R. T. Lord, B. M. Lunsky, K. Madisa, L. G. Magnus, J. P. L. Main, A. Makhaba, S. Makhathini, J. A. Malan, J. R. Manley, S. J. Marais, M. D. J. Maree, A. Martens, T. Mauch, K. McAlpine, B. C. Merry, R. P. Millenaar, O. J. Mokone, T. E. Monama, M. C. Mphego, W. S. New, B. Ngcebetsha, K. J. Ngoasheng, M. T.

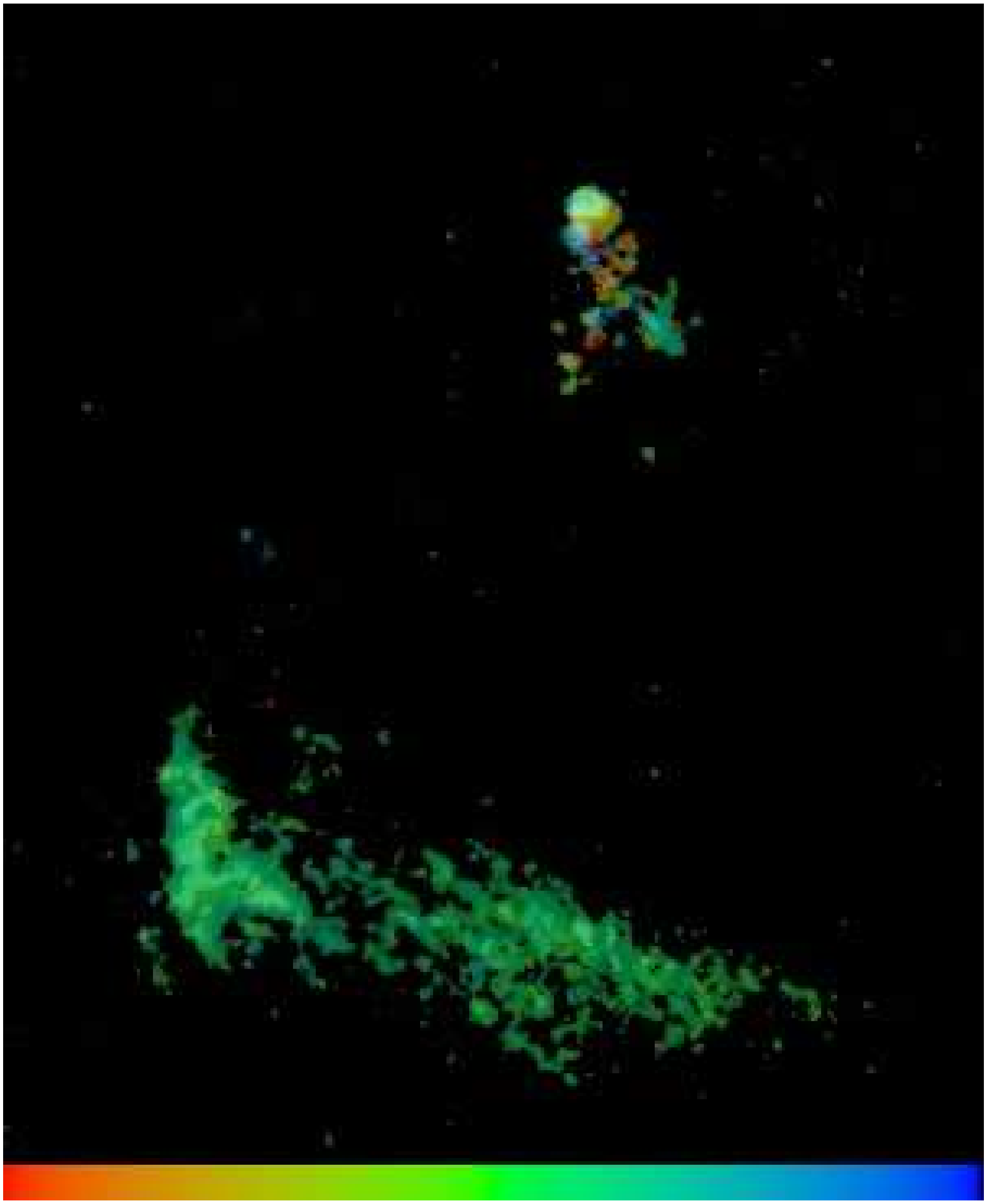

Fig. 16. Like Figure 15 but the region covering the halo (to the south) and AGN3 (to the north); the area shown is the upper right quadrant of Figure 12. Stretch is linear, red is 0 rad m^{-2} and blue is +100 rad m^{-2}.

Ockards, A. J. Otto, A. A. Patel, A. Peens-Hough, S. J. Perkins, N. M. Ramanujam, Z. R. Ramudzuli, S. M. Ratcliffe, R. Renil, A. Robyntjies, A. N. Rust, S. Salie, N. Sambu, C. T. G. Schollar, L. C. Schwardt, R. L. Schwartz, M. Serylak, R. Siebrits, S. K. Sirothia, M. Slabber, L. Sofeya, B. Taljaard, C. Tasse, A. J. Tiplady, O. Toruvanda, S. N. Twum, T. J. van Balla, A. van der Byl, C. van der Merwe, C. L. van Dyk, V. Van Tonder, R. Van Wyk, A. J. Venter, M. Venter, M. G. Welz, L. P. Williams, and B. Xaia, "The MeerKAT Galaxy Cluster Legacy Survey I. Survey Overview and Highlights," *arXiv e-prints*, p. arXiv:2111.05673, Nov. 2021.